

# On the Energy Analysis of Two-phase Flows Simulated with the Diffuse Interface Method

Ali Mostafavi<sup>a</sup>, Moahammadmahdi Ranjbar<sup>a</sup>, Vitaliy Yurkiv<sup>a</sup>, Alexander L. Yarin<sup>b</sup>, Farzad Mashayek<sup>a,\*</sup>

<sup>a</sup> *Department of Aerospace and Mechanical Engineering, University of Arizona, Tucson, AZ 85721, USA*

<sup>b</sup> *Department of Mechanical and Industrial Engineering, University of Illinois Chicago, Chicago, IL 60607, USA*

The Phase-Field Method (PFM) is employed to simulate two-phase flows, with the fully-coupled Cahn-Hilliard-Navier-Stokes (CHNS) equations governing the temporal evolution of the flow. The methodology is fundamentally based on the minimization of the total energy functional, accounting for diffusive and viscous dissipations in the presence of fluid flow. A novel perspective is presented by analyzing the interplay between kinetic energy, mixing energy, and viscous dissipation using the temporal evolution of the total energy functional. The classical surface energy is approximated with mixing energy under specific conditions, and the accuracy of this substitution is rigorously evaluated. The energy-based surface tension formulation, derived from the Korteweg stress tensor, demonstrates exceptional accuracy in capturing variations in mixing energy. These concepts are demonstrated by considering two benchmark problems: droplet oscillation and capillary jet breakup. Key findings include the identification of scenarios where curvature non-uniformity increases errors in surface energy approximation and the discovery of distinct energy dissipation patterns during jet breakup and droplet oscillations. The results highlight the robustness of the free energy-based PFM in accurately capturing complex interfacial dynamics, while providing practical strategies to ensure numerical consistency.

Keywords: Two-phase flow, Phase-Field Method, Cahn-Hilliard Navier-Stokes, Energy functional, Surface energy

## 1. Introduction

Multiphase flows of immiscible fluids, like oil and water, which inherently resist mixing, are prevalent in both natural and industrial systems. Notable applications where multiphase flows are crucial include drop impact (Halder et al., 2022; Mostafavi et al., 2023; Yarin, 2006), enhanced oil recovery (Alvarado and Manrique, 2010; Gbadamosi et al., 2019), additive manufacturing (Xia et al., 2018; Zhu and Yan, 2021), microfluidic (Mostafavi et al., 2024c; Zhao et al., 2016), and inkjet systems (Lohse, 2022; Rump et al.,

---

\* Corresponding author.  
*E-mail address:* mashayek@arizona.edu (F. Mashayek).

2022). Accurate modeling of such flows is highly sought after and has been the subject of substantial studies within the computational fluid dynamics (CFD) research community.

The three most widely used methodologies for modeling such flows are Volume-of-fluid (VOF) (Hirt and Nichols, 1981), Level-set (Sussman et al., 1994), and Phase-field methods (PFM). Typically, VOF and Level-set methodologies employ a sharp interface, while PFM adopts a diffusive interface with finite thickness. Classical methods for two-phase flow simulations involve interface matching conditions and surface tension localization. One natural advantage of phase-field methods is that they do not require special treatment at the interface. Instead, the method is based on thermodynamics arguments and free energy approximation to derive the flow's governing equations. The adoption of the PFM in two-phase flow simulations can be divided into Cahn-Hilliard (Cahn and Hilliard, 1958), Allen-Cahn (Allen and Cahn, 1972), and conservative second-order phase-field formulations (Chiu and Lin, 2011).

The original fourth-order Cahn-Hilliard equation ( $L^2$  gradient flow method) is in a conservative format, suitable for two-phase flow simulations. The non-conservative second-order Allen-Cahn equation ( $H^{-1}$  gradient flow method) requires special attention to maintain mass conservation, such as using Lagrange multipliers (RUBINSTEIN and STERNBERG, 1992). The use of the conservative second-order phase-field method is gaining popularity (Chiu and Lin, 2011; Jain et al., 2020; Mirjalili et al., 2020). The method is numerically advantageous as it yields conservative solutions, such as those governed by the Cahn-Hilliard equation, while reducing the complexity of the fourth-order derivative to a second-order derivative, as in the Allen-Cahn equation. As a result, it combines the conservative property of the Cahn-Hilliard equation with the lower derivative order of the Allen-Cahn equation, offering a more computationally efficient alternative. However, perhaps the most unique attribute of the original Cahn-Hilliard and Allen-Cahn phase-field equations is that they admit an energy law (Hua et al., 2011). They can predict the transient behavior of multiphase media by minimization of the energy functional. This characteristic sets the Cahn-Hilliard and Allen-Cahn phase-field equations apart from other interface-capturing and interface-tracking techniques, as well as conservative second-order phase field method, which do not adhere to a known energy law. The dissipative energy functional, which decreases monotonically over time, provides critical insights into the dynamics of multiphase systems and serves as a key indicator of numerical consistency. There have been considerable efforts in designing energy stable numerical schemes in phase-field simulations with diffusive interface approach in the literature, often without delving deeply into their physical interpretations especially in the fluid flow context.

Another advantage of phase-field methods is the existence of highly accurate approximation of surface tension force, known as energy-based surface tension formulation from the Korteweg stress tensor (Abels et al., 2012). The superior performance of the energy-based surface tension force, compared to the continuum surface force (CSF) model (Brackbill et al., 1992) and its localized variant, is discussed in

(Mirjalili et al., 2023). This approach reduces spurious currents and eliminates the need for direct surface curvature computation, offering an efficient and easy-to-implement method for estimating the surface tension force. Among the advantages, the phase-field method includes certain built-in assumptions that establish a link to classical methods for approximating surface energy. A key objective of this study is to conduct sanity checks and determine the conditions under which these assumptions hold most valid (Jacqmin, 1999; Yue et al., 2004).

The rest of the contents are organized as follows: In section 2, the governing equations and energy stability are formulated. Section 3 discusses the mixing energy and energy-based surface tension force formulation. In section 4, the derivation of the energy balance equation from the momentum balance equation is presented. Section 5 provides some information about the numerical framework and temporal and spatial discretization methods. In section 6, the suggested theories are applied to the droplet oscillation and capillary jet breakup benchmark problems. Conclusions on the findings of this work and future goals are included in section 7.

## 2. Governing equations

### 2.1. Coupled Cahn-Hilliard Navier Stokes equations

Considering a domain  $\Omega \subset \mathbb{R}^D$  ( $D \leq 3$ ) with the boundary  $\Gamma$ , The dynamics of the two-phase flow are governed by the coupled Cahn-Hilliard-Navier-Stokes equations, formulated in the absence of gravity, as follows:

$$\nabla \cdot \mathbf{u} = 0, \quad (1)$$

$$\rho \left( \frac{\partial \mathbf{u}}{\partial t} + \mathbf{u} \cdot \nabla \mathbf{u} \right) + (\mathbf{J} \cdot \nabla) \mathbf{u} = -\nabla P + \nabla \cdot \boldsymbol{\tau} + \mathbf{F}_{st}, \quad (2)$$

$$\frac{\partial c}{\partial t} + \mathbf{u} \cdot \nabla c = \nabla \cdot (M \nabla \psi), \quad (3)$$

$$\psi = \sigma \left( \frac{\partial f(c)}{\partial c} - \nabla^2 c \right). \quad (4)$$

Equations (1) and (2) describe the incompressibility condition and the momentum balance, with  $\mathbf{u}$  representing the fluid velocity vector,  $\boldsymbol{\tau} = \mu(\nabla \mathbf{u} + \nabla \mathbf{u}^T)$  the viscous stress tensor, and  $P$  the fluid pressure. The density,  $\rho$ , and viscosity,  $\mu$ , of the two-phase flow are both functions of the phase-field variable in the case of unmatched densities. Typically, linear or harmonic interpolations are employed to calculate material properties inside the computational domain for the one-fluid model. Note that it is not expected to obtain a perfect solenoidal velocity in the case of unmatched densities ( $\nabla \cdot \mathbf{u} \neq 0$ ). However, providing sufficient

mesh elements to decrease the density variation across the elements in the interface region can mitigate the issue. This is because equation (1) holds strictly for single-phase flows with constant density. Across the diffusive interface, smooth transition of material properties leads to a non-divergence-free velocity field.  $\mathbf{F}_{st}$  is the energy-based surface tension force and will be derived later.  $\mathbf{J} = \frac{\rho_2 - \rho_1}{2} M \nabla \psi$  represents the diffusive flux arising from the disparities between mass- and volume-averaged velocities and is proportional to the density difference between phases (Abels et al., 2012). Although  $(\mathbf{J} \cdot \nabla) \mathbf{u}$  is typically small and often neglected in engineering applications, it is retained in the momentum balance equation to ensure thermodynamic consistency, as highlighted in (Abels et al., 2012).

Equations (3) and (4) denote the split form of the advective Cahn-Hilliard phase-field equation, where  $c$  is the order parameter,  $\psi$  is the chemical potential,  $M$  is the phenomenological mobility coefficient,  $f(c)$  is the bulk free energy and  $\sigma$  is the mixing energy density. A macroscopic labeling function  $c$  is defined to differentiate between separate phases:  $c = 1$  represents fluid 1,  $c = -1$  indicates fluid 2,  $-1 < c < 1$  corresponds to the diffusive interface layer, with  $c = 0$  reflecting the fluid-fluid interface.

The mixing energy density per unit volume is given by

$$f_m(c, \nabla c) = \sigma \left( \frac{1}{2} |\nabla c|^2 + f(c) \right), \quad (5)$$

where,

$$f(c) = \frac{(c^2 - 1)^2}{4\xi^2}, \quad (6)$$

is the double-well potential, with  $\xi$  representing the capillary width, also known as the interface thickness. This equation recognizes a phobic bulk component,  $\sigma f(c)$ , which represents the tendency for phase separation, and a philic surface component,  $\frac{\sigma}{2} |\nabla c|^2$ , which implies the mixing tendency (Yue et al., 2004).

The original Cahn-Hilliard equation governs the evolution of the conserved variable  $c$  by facilitating the dissipation of the free energy functional,

$$\mathcal{F} = \int_{\Omega} (f_m(c, \nabla c)) d\Omega. \quad (7)$$

The free energy functional  $\mathcal{F}$  (also known as the Ginzburg-Landau free energy) represents the total free energy of the system over the domain  $\Omega$ . It consists of the local free energy density  $f(c)$ , which represents

the bulk free energy and the gradient energy density  $f_{gr} = \frac{\sigma}{2} |\nabla c|^2$ , both of which act exclusively at the diffusive interface. Hence, the total mixing energy of the system, when no additional source of energy is present, is  $\mathcal{F}$ . Commonly, the double-well free function is used to delineate the local free energy  $f(c)$  in two-phase flow simulations (Eq. (6)). The chemical potential  $\psi$  is defined as the variational derivative of the total free energy of the system  $\mathcal{F}$  with respect to the phase-field variable, i.e.,  $\psi = \delta\mathcal{F}/\delta c$ . This formulation ensures that in the absence of fluid flow, the multiphase media reaches an equilibrium state by minimizing its free energy.

## 2.2. Energy stability

The standard Cahn-Hilliard equation predicts the evolution of a conserved variable based on the minimization of the total free energy of a multiphase system. However, in multiphase fluid flows, additional forms of energy are involved, including the kinetic energy and potential energy of the flow. The link between the momentum balance and phase-field equations is established implicitly by taking the inner product of Eq. (3) with  $-\psi$ , Eq. (4) with  $\partial c/\partial t$  and Eq. (2) with  $\mathbf{u}$ , and then summing the relations, obtaining the following dissipative energy law under zero-gravity condition (Khanwale et al., 2023; Shen and Yang, 2015; Yue et al., 2004):

$$\frac{dE_{tot}}{dt} = - \int_{\Omega} \left( \frac{\mu}{2} \|\nabla \mathbf{u}\|_F^2 + M \|\nabla \psi\|^2 \right) d\Omega, \quad (8)$$

where,

$$E_{tot} = \int_{\Omega} \left( \frac{1}{2} \rho \|\mathbf{u}\|^2 + f_m(c, \nabla c) \right) d\Omega = E_k + E_m. \quad (9)$$

The norms designated in Eqs. (8) and (9) are the Frobenius matrix norm and the Euclidean vector norm, respectively. These norms are, respectively, defined as follows (Khanwale et al., 2023):

$$\|\nabla \mathbf{u}\|_F^2 = \sum_i \sum_j \left| \frac{\partial u_i}{\partial x_j} \right|^2, \quad \|\mathbf{u}\|^2 = \sum_i |u_i|^2. \quad (10)$$

$E_{tot}$  is the energy functional for the two-phase flow, composed of kinetic energy  $E_k$  and total free/mixing energy  $E_m$  and is dissipated through viscous and diffusive dissipations. Cahn-Hilliard two-phase flow simulations uniquely minimize  $E_{tot}$ , setting them apart from methods like VOF, Level-set, and second-

order phase-field, which lack an energy law. A portion of the phase-field literature has focused on developing numerical schemes possessing energy stability, meaning they exhibit dissipative behavior over time. Various numerical schemes such as convex splitting (Eyre, 1998), linear stabilization (Shen et al., 2016), invariant energy quadratization (Yang, 2016) and scalar auxiliary variable (Shen et al., 2018) have been developed (Yue, 2020). The energy stability feature must be preserved in different numerical schemes unconditionally. Since the main purpose of this paper is to offer new perspectives on studying two-phase flow dynamics from an energy standpoint, the time derivative of the total energy,  $\dot{E}_{tot}$ , is also monitored, as it holds significant meaning in the context of fluid flow. It directly relates viscous and diffusive dissipations to the energy functional and highlights the stages at which the flow is predominantly dissipative.

### 3. Mixing energy and capillary force

Considering a 1D case, where an interface is at equilibrium without fluid flow ( $\mathbf{u} = 0$ ), the diffusive flux must vanish at the interface, i.e.,  $\psi = \delta\mathcal{F}/\delta c = 0$  (Ding and Spelt, 2007; Yue et al., 2004). This results in the following equation describing the conserved order parameter at equilibrium:

$$\sigma \left( -\frac{d^2c}{dx^2} + \frac{\partial f(c)}{\partial c} \right) = 0, \quad (11)$$

yielding  $c(x) = \tanh(x/\sqrt{2}\xi)$ . Note that in this scenario, the bulk energy derivative and gradient energy effectively cancel each other out from Eq. (11). The distribution of the order parameter,  $c$ , and the bulk free energy density,  $f(c)$ , for various interfacial thicknesses at the equilibrium state is given in Fig. 1 (a) and Fig. 1 (b), respectively.

The connection between the diffuse interface approach and the classical concept of interfacial tension is established by equating the total free energy with the traditional surface energy, as follows (Yue et al., 2004):

$$\gamma = \sigma \int_{-\infty}^{\infty} \left\{ \frac{1}{2} \left( \frac{dc}{dx} \right)^2 + f(c) \right\} dx. \quad (12)$$

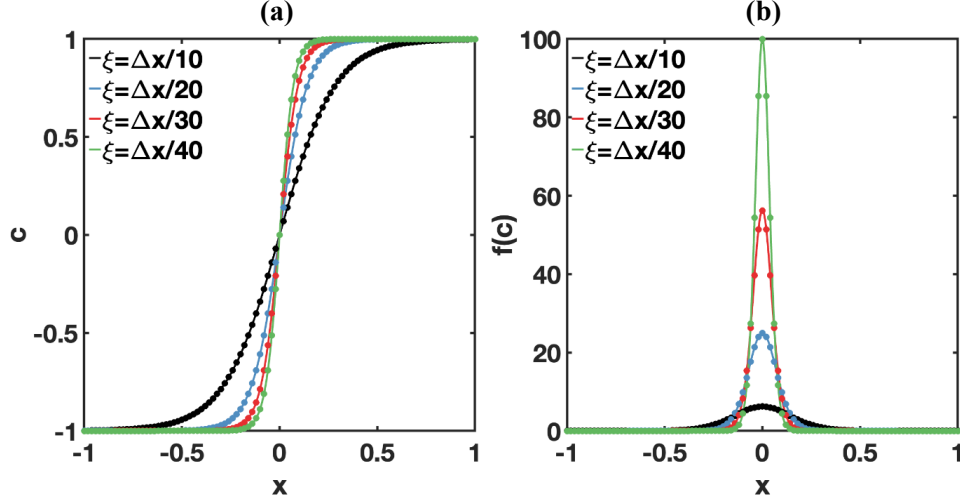


**Fig. 1.** Results of the 1D interface at equilibrium without fluid flow. Displayed in the panels are (a) the equilibrium profile of the order parameter and (b) the bulk free energy for various values of the interfacial thickness.

Upon substituting the equilibrium profile  $c(x) = \tanh(x/\sqrt{2}\xi)$  for the order parameter into Eq. (12) and performing integration, the following relationship between the mixing energy density  $\sigma$ , and the interfacial surface tension coefficient  $\gamma$  holds:

$$\sigma = \frac{3}{2\sqrt{2}}\gamma\xi. \quad (13)$$

It is important to emphasize that Eq. (13) yields exact results regardless of the interfacial thickness. Despite this, its applicability is restricted to a specific 1D condition without fluid flow at equilibrium, where there is no gradient in the chemical potential. In practical applications, we are interested to know the transient behavior of two-phase flows in the presence of the fluid flow. With phase-field modeling, we are still required to use Eq. (13) to approximate the surface energy. It is of broad interest to examine how well Eq. (13) holds when simulating the transient behavior of two-phase flows and approximating the classical surface energy using a free energy approach. To the best of our knowledge, such investigations have not been the subject of rigorous study in the context of phase-field two-phase flow simulations.

Now, let us reproduce the surface tension force and modify the momentum balance in Eq. (2) slightly. The derivation is prerequisite for consolidating some arguments in energy exchange analysis. In the phase-field methods, the surface tension force is calculated through the second law of thermodynamics (Mirjalili et al., 2023). It is proportional to the divergence of the so-called Korteweg stress tensor  $\nabla \cdot (\nabla c \otimes \nabla c)$

where  $\otimes$  is the tensor product) which satisfies the energy dissipative law (Anderson et al., 1998) and is obtained as follows (Mirjalili et al., 2023):

$$\sigma \nabla \cdot (\nabla c \otimes \nabla c) = \sigma (\nabla c \nabla^2 c + \nabla c \cdot \nabla (\nabla c)) = \sigma \left( \nabla c \nabla^2 c + \frac{1}{2} \nabla (\nabla c \cdot \nabla c) \right). \quad (14)$$

The above equation can be modified such that the chemical potential,  $\psi$ , appears by adding and subtracting  $f' \nabla c$  where  $f' = \partial f(c) / \partial c$ :

$$\sigma \nabla \cdot (\nabla c \otimes \nabla c) = \sigma \left( \nabla c \nabla^2 c + \frac{1}{2} \nabla (\nabla c \cdot \nabla c) + f' \nabla c - f' \nabla c \right). \quad (15)$$

Now let us further simplify by invoking equation (4):

$$\sigma \nabla \cdot (\nabla c \otimes \nabla c) = \sigma \nabla c (\nabla^2 c - f') + \sigma \left( \frac{1}{2} \nabla (\nabla c \cdot \nabla c) + f' \nabla c \right). \quad (16)$$

Note that  $\psi = \sigma(f' - \nabla^2 c)$ . It is desirable to put the second term on the right-hand side of Eq. (16) inside the  $\nabla$  operator, which results in:

$$\sigma \nabla \cdot (\nabla c \otimes \nabla c) = -\psi \nabla c + \sigma \nabla \left( \frac{1}{2} \nabla c \cdot \nabla c + f \right). \quad (17)$$

Putting the Korteweg stress tensor on the right-hand side of the momentum balance equation changes its sign. The second term on the right-hand side of equation (17) can be absorbed on the fluid pressure gradient term  $\nabla P$ . Therefore, the followings are obtained for the volumetric surface tension force approximation and modified pressure:

$$\mathbf{F}_{st} = \psi \nabla c, \quad (18)$$

$$p = P + \sigma \left( \frac{1}{2} \nabla c \cdot \nabla c + f \right). \quad (19)$$



Consequently, the energy-based surface tension force is derived, and the fluid pressure  $P$  in Eq. (2) is replaced by the modified pressure  $p$ . Note that all the equations are expressed using the  $\nabla$  operator, making them applicable to 2D, 2D axisymmetric, and 3D flows.

#### 4. Dynamics of the energy exchange in two-phase flows

Another way to analyze two-phase flows from an energy perspective is by taking the dot product of the momentum balance equation with the velocity vector  $\mathbf{u}$ , which yields:

$$\rho \mathbf{u} \cdot \left( \frac{\partial \mathbf{u}}{\partial t} + \mathbf{u} \cdot \nabla \mathbf{u} \right) + \mathbf{u} \cdot (\mathbf{J} \cdot \nabla) \mathbf{u} = -\mathbf{u} \cdot \nabla p + \mathbf{u} \cdot (\nabla \cdot \mu (\nabla \mathbf{u} + \nabla \mathbf{u}^T)) + \mathbf{u} \cdot (\mathbf{F}_{st}). \quad (20)$$

Taking the surface/volume integral of Eq. (20) leads to:

$$\begin{aligned} \int_{\Omega} \left( \rho \mathbf{u} \cdot \frac{\partial \mathbf{u}}{\partial t} + \rho \mathbf{u} \cdot (\mathbf{u} \cdot \nabla \mathbf{u}) + \mathbf{u} \cdot (\mathbf{J} \cdot \nabla) \mathbf{u} \right) d\Omega \\ = \int_{\Omega} \left( -\mathbf{u} \cdot \nabla p + \mathbf{u} \cdot (\nabla \cdot \mu (\nabla \mathbf{u} + \nabla \mathbf{u}^T)) + \mathbf{u} \cdot \mathbf{F}_{st} \right) d\Omega. \end{aligned} \quad (21)$$

For the sake of simplicity, let us consider two-phase flows with matched densities and viscosities first and neglect gravity. Note that diffusive flux is zero for the matched density cases ( $\mathbf{J} = \mathbf{0}$ ). By virtue of the divergence-free velocity field assumption ( $\nabla \cdot \mathbf{u} = 0$ ), the pressure gradient and advection terms can be rewritten as,

$$\mathbf{u} \cdot \nabla p = \nabla \cdot (p \mathbf{u}), \quad \rho \mathbf{u} \cdot (\mathbf{u} \cdot \nabla \mathbf{u}) = \frac{1}{2} \nabla \cdot (\rho \mathbf{u} |\mathbf{u}|^2). \quad (22)$$

Theoretically, the advection term  $\int_{\Omega} \frac{1}{2} \nabla \cdot (\rho \mathbf{u} |\mathbf{u}|^2) d\Omega$  and the modified pressure gradient term  $\int_{\Omega} \nabla \cdot (p \mathbf{u}) d\Omega$  should give zero under specific conditions. This can be shown with the application of the divergence theorem once the velocity field is supplemented with periodic boundary conditions or the following on the domain boundaries:

$$\mathbf{u}|_{\Gamma} = 0, \quad \frac{\partial \mathbf{u}}{\partial \mathbf{n}}|_{\Gamma} = 0, \quad (23)$$

where  $\mathbf{n}$  is the unit normal vector to  $\Gamma$ . Also, the first term on the left-hand side of Eq. (21) is the time derivative of the kinetic energy  $E_k$ , which will be referred to as  $\partial E_k / \partial t$  from this point forward. Note that there is no spatial or temporal change in  $\rho$  for the matched density case, therefore,

$$\frac{\partial E_k}{\partial t} = \partial_t \left( \rho, \frac{|\mathbf{u}|^2}{2} \right) = (\rho \mathbf{u}_t, \mathbf{u}), \quad (24)$$

where  $(\cdot, \cdot)$  indicates the inner product in  $L^2(\Omega)$ . Hence, Eq. (21) reduces to:

$$\frac{\partial E_k}{\partial t} = \int_{\Omega} (\mathbf{u} \cdot (\nabla \cdot \mu(\nabla \mathbf{u} + \nabla \mathbf{u}^T)) + \mathbf{u} \cdot \mathbf{F}_{st}) d\Omega. \quad (25)$$

Let us denote the viscous dissipation term by  $\Phi_v = \mathbf{u} \cdot (\nabla \cdot \mu(\nabla \mathbf{u} + \nabla \mathbf{u}^T))$ . Note that for a single-phase flow, the derivative order can be reduced by applying the divergence theorem. Despite this, we keep this term intact to apply it later to the cases of unmatched densities and viscosities. For completeness, the expressions for  $\Phi_v$  are provided in both  $xy$  (Cartesian) and  $rz$  (axisymmetric) coordinates:

$$\Phi_{v,xy} = \mu \left( \mathbf{u}_x \left( \frac{\partial^2 \mathbf{u}_x}{\partial x^2} + \frac{\partial^2 \mathbf{u}_x}{\partial y^2} \right) + \mathbf{u}_y \left( \frac{\partial^2 \mathbf{u}_y}{\partial x^2} + \frac{\partial^2 \mathbf{u}_y}{\partial y^2} \right) \right), \quad (26)$$

$$\Phi_{v,rz} = \mu \left( \mathbf{u}_r \left( \frac{\partial^2 \mathbf{u}_r}{\partial r^2} + \frac{\partial^2 \mathbf{u}_r}{\partial z^2} + \frac{1}{r} \frac{\partial \mathbf{u}_r}{\partial r} - \frac{\mathbf{u}_r}{r^2} \right) + \mathbf{u}_z \left( \frac{\partial^2 \mathbf{u}_z}{\partial r^2} + \frac{\partial^2 \mathbf{u}_z}{\partial z^2} + \frac{1}{r} \frac{\partial \mathbf{u}_z}{\partial r} \right) \right). \quad (27)$$

Due to the presence of the second-order derivatives of the fluid velocity, first-order Lagrange elements can no longer be used for velocity approximation as they return zero for second-order derivatives unless the solution is accurately reconstructed with higher-order shape functions, or the derivative order is reduced by the application of the divergence theorem. Alternatively, the velocity could be discretized using at least a second-order approximation to accurately compute the viscous dissipation in the formulated approach. The schematic of a finite element used in this work is illustrated in Fig. 2. Linear shape functions are used for  $p$ ,  $c$  and  $\psi$ , while quadratic shape functions are used for  $\mathbf{u}$  to directly compute  $\Phi_v$ .

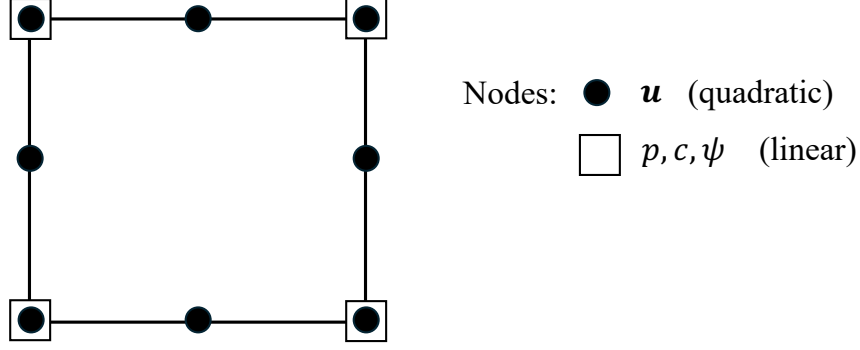


**Fig. 2.** A diagram of 2D Quad8 libMesh Lagrange element (Kirk et al., 2006) used for spatial discretization. Second-order shape functions are utilized for the velocity approximation, while other nonlinear variables are interpolated using linear shape functions.

Spatial integration can produce numerical errors. The most accurate way for performing the integration in Eq. (21) is to use Gaussian quadrature points rather than nodal points. Subsequently, taking the temporal integral of Eq. (25) yields:

$$E_{k,t} - E_{k,0} = \int_0^t \int_{\Omega} \Phi_v d\Omega dt + \int_0^t \int_{\Omega} \mathbf{u} \cdot \mathbf{F}_{st} d\Omega dt, \quad (28)$$

which relates the change of the kinetic energy to the work of viscous ( $E_v$ ) and surface tension forces. From intuition, the change in kinetic energy is related to the change of surface energy and viscous dissipation. Therefore, it is anticipated that the surface tension force's work represents the change in the surface (also known as potential) energy of the flow. It is of general interest to show the comparison between  $\int_0^t \int_{\Omega} \mathbf{u} \cdot \mathbf{F}_{st} d\Omega dt$  which is the work of surface tension force and the variation of free energy functional/mixing energy  $\int_{\Omega} f_m(c, \nabla c) d\Omega$  from an initial stage. Additionally, for a given interface, the surface energy is equal to the product of the surface tension coefficient and the surface area. Thus, the surface energy is perhaps overdetermined in two ways. Ideally, they should be exactly equal; however, note that the derivation in Eq. (12) is for an extremely specific condition.

The extension of the arguments made thus far to two-phase flows with variable density and viscosity is somewhat different. Considering Eq. (22), the pressure gradient term can still be put in the  $\nabla$  operator and converted into a boundary integral using the divergence theorem and subsequently eliminated. The main difference is that  $\partial E_k / \partial t$  does contain time derivative of density which is non-zero for flows with unmatched densities. By using linear interpolation for  $\rho$  and defining  $\mathbf{J}$  as follows,

$$\rho(c) = \frac{\rho_1 - \rho_2}{2}c + \frac{\rho_1 + \rho_2}{2}, \quad \mathbf{J} = \frac{\rho_2 - \rho_1}{2}M\nabla\psi, \quad (29)$$

the following equation is obtained for the temporal change of density from Eqs. (1), (3), (29) (Shen and Yang, 2015):

$$\frac{\partial \rho}{\partial t} + \nabla \cdot (\rho \mathbf{u}) + \nabla \cdot \mathbf{J} = 0. \quad (30)$$

Abels et al. demonstrated that the individual masses of the distinct phases remain conserved with this formulation (Abels et al., 2012). In the case of two-phase flows with unmatched densities,  $\partial E_k / \partial t$  is calculated as (Shen and Yang, 2015):

$$\begin{aligned} \partial_t \left( \rho, \frac{|\mathbf{u}|^2}{2} \right) &= (\rho \mathbf{u}_t, \mathbf{u}) + \left( \rho_t, \frac{|\mathbf{u}|^2}{2} \right) = (\rho \mathbf{u}_t, \mathbf{u}) - \left( \nabla \cdot (\rho \mathbf{u}) + \nabla \cdot \mathbf{J}, \frac{|\mathbf{u}|^2}{2} \right) \\ &= (\rho \mathbf{u}_t + \rho \mathbf{u} \cdot \nabla \mathbf{u} + \mathbf{J} \cdot \nabla \mathbf{u}, \mathbf{u}). \end{aligned} \quad (31)$$

Equation (31) relates the temporal change in the kinetic energy to the left-hand side of Eq. (21). The term  $(\rho \mathbf{u}_t, \mathbf{u})$  represents the change in the kinetic energy due to the variation in velocity, while  $(\rho \mathbf{u} \cdot \nabla \mathbf{u} + \mathbf{J} \cdot \nabla \mathbf{u}, \mathbf{u})$  accounts for the change in kinetic energy due to the variation in density. Although due to the density variations the expression for  $\partial E_k / \partial t$  is different for matched and unmatched cases, equation (28) is applicable to both. Energy analysis have been extensively performed for single-phase flows (Ranjbar et al., 2024), but they are lacking in the Cahn-Hilliard-Navier-Stokes (CHNS) two-phase flow literature. In the diffuse-interface picture, two-phase flows are treated as a one-fluid model, and the conservation laws are solved in the two-phase flow domain. Note that omitting  $(\mathbf{J} \cdot \nabla) \mathbf{u}$  from the momentum balance equation invalidates Eq. (31) and introduces thermodynamic inconsistency.

In summary, this section introduces several approaches to analyzing two-phase flows from an energy perspective. Additionally, some methods for assessing the numerical accuracy and consistency of the obtained solutions are discussed. The next section outlines the details of the computational framework, followed by a discussion of the results in section 6.

## 5. Numerical methods

The equation system (1)-(4) is solved by the finite element method using the continuous Galerkin discretization within the MOOSE framework (Permann et al., 2020). First-order  $Q1$  elements are used for

$p$ ,  $c$ ,  $\psi$ , while second-order  $Q2$  are used for  $\mathbf{u}$  to accurately calculate the domain integral for the viscous dissipation term as discussed previously. Furthermore, the use of second-order velocity approximation results in a better conservation of the momentum equation compared to the first-order approximation. To eliminate the saddle point nature of the continuity equation, an on-diagonal dependency to  $p$  is introduced. A consistent Pressure-Stabilized Petrov-Galerkin (PSPG) stabilization term is added to Eq. (1) as  $(\nabla \hat{p}, -\frac{\tau_{\text{PSPG}}}{\rho} \mathbf{R}^{(u)})$  where  $\hat{p}$  is the typical  $C^0$  finite element test function for  $p$ ,  $\tau_{\text{PSPG}}$  is the mesh- and solution-dependent stabilization parameter, and  $\mathbf{R}^{(u)}$  the strong residual term of Eq. (2) (Peterson et al., 2018). It is not expected that this stabilization parameter exacerbates the divergence-free velocity field as  $\mathbf{R}^{(u)}$  is minimized to zero. Thus, providing a small enough tolerance for the residual of the momentum balance equation ensures that  $\mathbf{R}^{(u)}$  is negligible. The full weak form of the governing equations can be expressed as:

$$\left( \rho \frac{D\mathbf{u}}{Dt} + \mathbf{J} \cdot \nabla \mathbf{u}, \hat{\mathbf{u}} \right)_{\Omega} - (\psi \nabla \mathbf{c}, \hat{\mathbf{u}})_{\Omega} + (-p\mathbf{I} + \boldsymbol{\tau}, \nabla \hat{\mathbf{u}})_{\Omega} - (\mathbf{n} \cdot (-p\mathbf{I} + \boldsymbol{\tau}), \hat{\mathbf{u}})_{\Gamma} = 0, \quad (32)$$

$$-(\nabla \cdot \mathbf{u}, \hat{p})_{\Omega} - \left( \frac{\tau_{\text{PSPG}}}{\rho} \mathbf{R}^{(u)}, \nabla \hat{p} \right)_{\Omega} = 0, \quad (33)$$

$$\left( \psi - \sigma \frac{\partial f}{\partial c}, \hat{c} \right)_{\Omega} - (\sigma \nabla \mathbf{c}, \nabla \hat{c})_{\Omega} + (\mathbf{n} \cdot (\sigma \nabla \mathbf{c}), \hat{c})_{\Gamma} = 0, \quad (34)$$

$$\left( \frac{\partial c}{\partial t}, \hat{\psi} \right)_{\Omega} + (\mathbf{u} \cdot \nabla \mathbf{c}, \hat{\psi})_{\Omega} + (M \nabla \psi, \nabla \hat{\psi})_{\Omega} - (\mathbf{n} \cdot (M \nabla \psi), \hat{\psi})_{\Gamma} = 0. \quad (35)$$

Note that the variables shown with  $\hat{\cdot}$  are the corresponding test functions. The governing equations are solved in a fully-coupled and fully-implicit manner altogether. The temporal discretization is performed using a finite difference approximation, with time integration implemented through the Backward Differentiation Formula of order 2 (BDF2). This scheme provides second-order accuracy in time. The nonlinear system is solved using the Newton method (Gaston et al., 2009). At each Newton iteration, the resulting linearized system is solved using the MULTifrontal Massively Parallel Sparse direct Solver (MUMPS), which efficiently handles large linear systems via LU factorization.

All the simulations in this work significantly benefit from applying the adaptive mesh refinement (AMR) at the interface. Although it provides sufficient resolution and effectively models thin interfaces, the interpolation error introduced during the mesh coarsening process is a drawback. In our previous work, a

Lagrange multiplier was introduced to reduce the mesh-coarsening effects on the global conservation of phase-field variable within the machine precision error with accurate physical outcomes (Mostafavi et al., 2024b). The simulations leverage parallel computing capabilities by utilizing the METIS package for efficient domain partitioning, which dynamically optimizes the workload distribution across multiple processors each time step (Karypis and Kumar, 1997). An illustration of the computational mesh, leveraging AMR and parallel computing with the METIS domain partitioner package, is presented in Fig. 3.

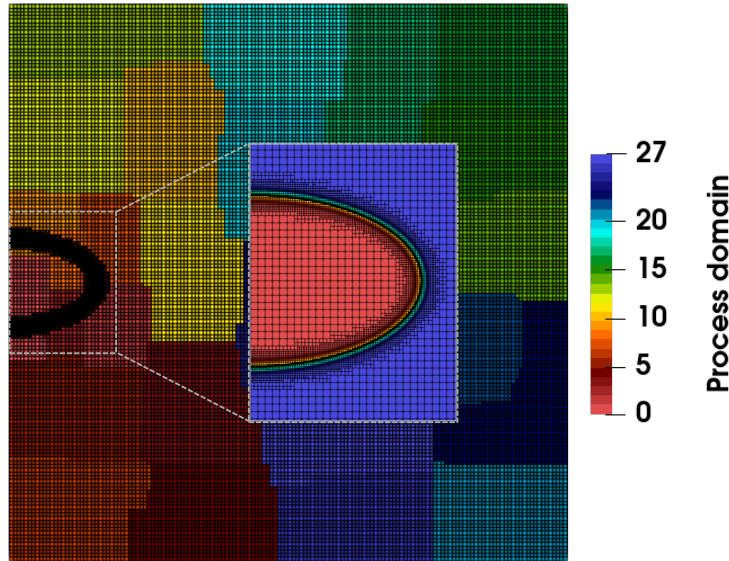


**Fig. 3.** Representation of AMR at the interface and domain partitioning into 28 zones. The figure displays the entire domain, which consists of a  $150 \times 150$  base mesh, where regions with the same color are handled by the same processor. The zoomed inset highlights the mesh near the interfacial region with three levels of AMR, while the solid black line represents the contour of  $c = 0$ .

## 6. Results and discussions

### 6.1. Matched-density droplet oscillation

The oscillation dynamic of an initially ellipsoidal droplet in a two-phase medium is used as a benchmark problem for the energy analysis. The arguments are extendable to many types of two-phase flows with the same underlying physics. A schematic of the computational domain is provided in Fig. 4, depicting a square domain of size  $8R \times 8R$ , where  $R$  represents the volume-equivalent radius of the droplet. Large-amplitude oscillations of an initially oblate spheroidal droplet with an initial aspect ratio of 2 are simulated. The analysis starts with matched density and viscosity and is later expanded to different material properties. In Fig. 4, the  $z$ -axis is the axis of symmetry, and all variables are supplemented with zero-flux boundary conditions, which does not require special treatment in finite element method, except for  $\mathbf{u}_r = 0$  at the axis

of symmetry. This set of boundary conditions theoretically zeroes out  $\int_{\Omega} -\mathbf{u} \cdot \nabla p \, d\Omega$  and  $\int_{\Omega} \rho \mathbf{u} \cdot (\mathbf{u} \cdot \nabla \mathbf{u}) \, d\Omega$ .

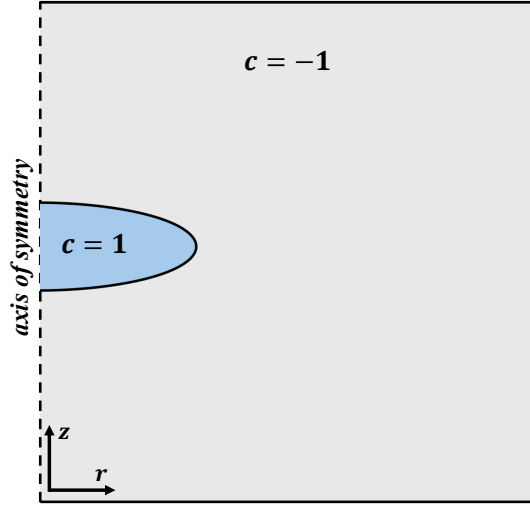


**Fig. 4.** The schematic of the problem setup to study the oscillatory behavior of an axisymmetric droplet. Initially, the perturbed spheroid has an oblate shape with an aspect ratio of 2.

The fluid parameters are assumed to be  $\rho = 10^3 \text{ kg/m}^3$ ,  $\mu = 10^{-3} \text{ Pas}$  and  $\gamma = 0.067 \text{ N/m}$  (Mashayek and Ashgriz, 1995). The oscillation dynamics is commonly studied by specifying the Reynolds number ( $Re = \rho UR/\mu$ ) and the Weber number ( $We = \rho U^2 R/\gamma$ ) in the absence of gravity and external forces. For the case of matched density and viscosity, the Reynolds number is set to  $Re = 200$ . The velocity scale  $U$  is obtained by setting the Weber number to  $We = 1$ . The radius of the unperturbed spherical droplet, which also serves as the characteristic length, is given by:

$$\tilde{R} = \frac{Re^2 \mu^2}{We \rho \gamma}. \quad (36)$$

The characteristic velocity, time, energy, and energy rate are defined, respectively, as follows:

$$\tilde{U} = \frac{Re \mu}{\rho \tilde{R}}, \quad \tilde{t} = \frac{\tilde{R}}{\tilde{U}}, \quad \tilde{E} = \frac{1}{2} \rho \tilde{U}^2 \mathcal{V}, \quad \tilde{\dot{E}} = \frac{\tilde{E}}{\tilde{t}}, \quad (37)$$

where  $\mathcal{V}$  is the volume of the spherical droplet. These characteristic numbers are used to render the results dimensionless, although the governing equations are solved in a dimensional form.

The mobility parameter remains constant, and the interfacial thickness is chosen as  $\xi = R/20$ . In Fig. 5 (a), the volume integration in Eq. (21) is performed at the quadrature points. The plots show the individual

dimensionless volume integrals of  $\rho \mathbf{u} \cdot \partial \mathbf{u} / \partial t$ ,  $\rho \mathbf{u} \cdot (\mathbf{u} \cdot \nabla \mathbf{u})$ ,  $-\mathbf{u} \cdot \nabla p$ ,  $\Phi_v$  and  $\mathbf{u} \cdot \mathbf{F}_{st}$ , which are obtained by taking the dot product of  $\mathbf{u}$  and the momentum equation. As expected from the application of the divergence theorem,  $\rho \mathbf{u} \cdot (\mathbf{u} \cdot \nabla \mathbf{u})$  and  $-\mathbf{u} \cdot \nabla p$  yield values that are very close to zero. The comparison of the terms on the left-hand side (time derivative of the kinetic energy) and the right-hand side (time derivative of the viscous dissipation and work of surface tension force) is shown in Fig. 5 (b). The figure shows an excellent balance between the energy terms. This consistency indicates the adequate accuracy of the code regarding the energy balance, momentum conservation, and solenoidal velocity field. It is imperative to mention that results plotted in Fig. 5 are energy rates and non-dimensionalized with  $\tilde{E}$ .

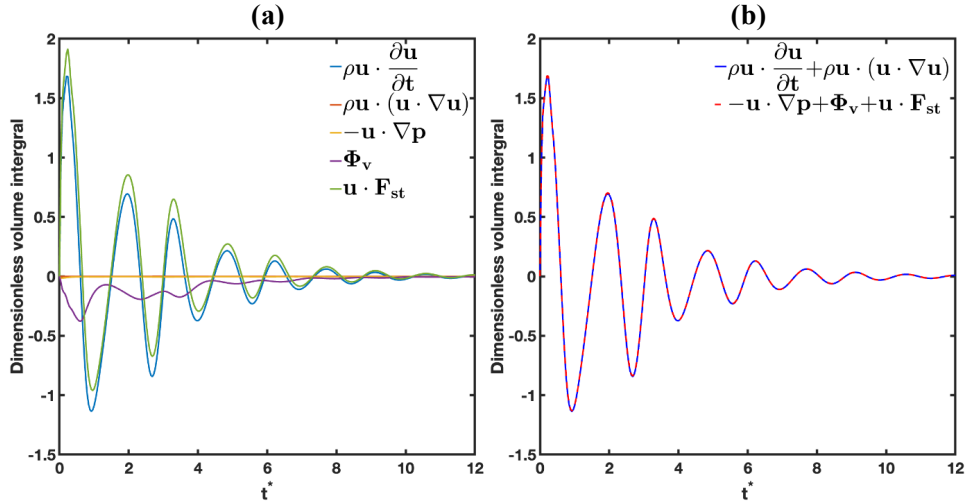


**Fig. 5.** The results for the energy conservation analysis: (a) the individual contribution from each term in the energy equation (Eq. (21)) and (b) the energy balance during the simulation.

Upon demonstrating the reliable solution to the Navier-Stokes equation in our numerical framework, the effects of the interfacial thickness on different forms of energy are explored. Four different values for the capillary width are considered as  $\xi = R/10, R/20, R/30, R/40$ . First, the effect of  $\xi$  on  $E_{tot}^*$  is reported. From the energy stability in Eq. (8), it is expected that  $E_{tot}^*$  monotonically decreases over time and  $dE_{tot}^*/dt < 0$ . From Fig. 6 (a) the dissipative energy feature is evident in the obtained solutions, indicating that the solution to the coupled CHNS equations satisfies the momentum conservation and is energy stable. It is crucial to conduct energy stability and energy conservation checks together before drawing any conclusions about the system's energy balance. Once the solution is confirmed to be both conservative and energy stable, the interrelation between the kinetic energy, the viscous dissipation, and the mixing energy can be accurately expressed using the results plotted in Fig. 6 (b)-(d). All energy plots imply that the oscillation dynamics are incorrectly predicted when  $\xi = R/10$ , as evidenced by discrepancies in the peaks of both kinetic and surface energies. However, when the interfacial thickness is reduced to below  $\xi = R/30$ , the energy components exhibit reasonable agreement.



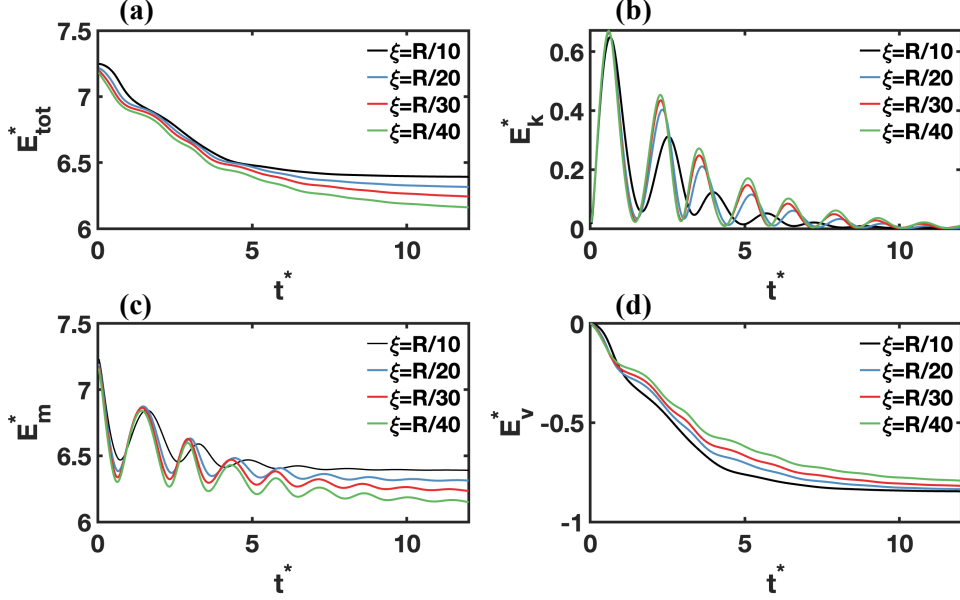


**Fig. 6.** The effect of the interfacial thickness on non-dimensional (a) total energy, (b) kinetic energy, (c) mixing energy and (d) viscous dissipation.

## 6.2. Unmatched-density droplet oscillation

The extension of the analysis to cases with unmatched densities is straightforward. The primary difference arises from the change in the kinetic energy, which is now governed by Eq. (31) instead of Eq. (24), due to the time dependence of the density. It might be considered a limitation of the current phase-field formulation that the incompressibility condition ( $\nabla \cdot \mathbf{u} = 0$ ) is enforced for continuity, despite the occurrence of density variation at the interface. Yue (Yue, 2020) considered the effects of compressibility and found that they are confined to the interfacial region, with minimal impact on the macroscopic flow in oscillating droplets with contact angle hysteresis on a solid surface.

The problem setup follows the same procedure as described in section 6.1, except for  $Re = 20, \rho_1/\rho_2 = 10, \mu_1/\mu_2 = 2$ . This section examines the effect of the interfacial thickness on the total energy and compares between mixing and surface energies.

As shown in Fig. 7 (a) and Fig. 7 (b), energy stability is maintained across all capillary widths. The entire CHNS theory is rooted in the minimization of the energy functional ( $E_{tot}$ ). When examining  $E_{tot}^*$ , it becomes evident that the flow is dissipative in nature, primarily due to viscous and diffusive dissipations. Another notable aspect of the flow, revealed by studying  $E_{tot}^*$ , is its equilibrium state. At equilibrium, the fluid velocity approaches zero, eliminating viscous dissipation; however, unphysical diffusive dissipation may still persist due to the interface regularization term ( $\nabla \cdot (M\nabla\psi)$ ) in the advective Cahn-Hilliard equation. Consequently, numerical simulations can be terminated once viscous dissipation ceases to be significant and  $E_{tot}^*$  reaches a plateau.

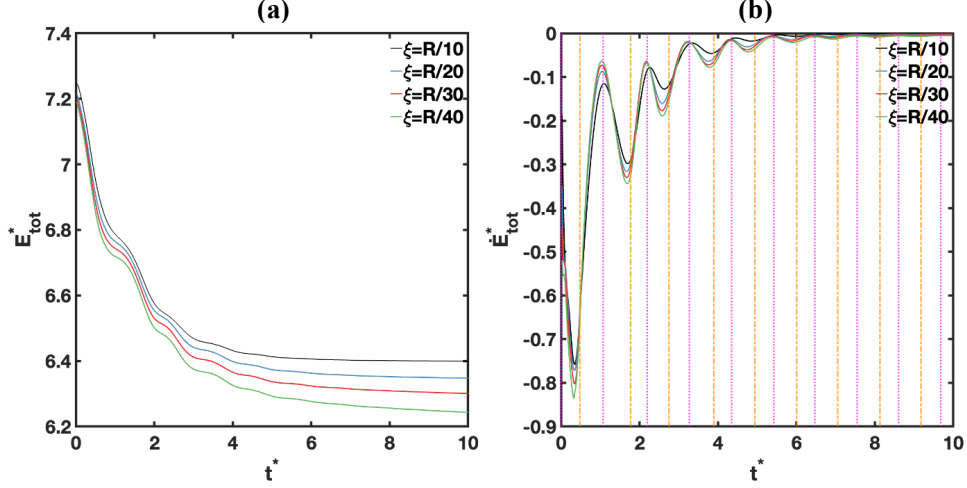


**Fig. 7.** The results for the droplet oscillation with unmatched densities. (a) The time variation of the total energy and (b) the rate of change of the total energy in time. The magenta dotted lines indicate the moments with maximum/minimum aspect ratios, while the orange dash-dotted lines show when the aspect ratio is unity.

Examining  $\dot{E}_{tot}^*$ , on the other hand, provides additional information about the fluid flow. Since it contains the effects of the viscous dissipation (Eq. (8)), it can reveal that at which stage the dissipative effects are more pronounced. At the start, with an initial aspect ratio of 2, the droplet has an elongated ellipsoidal shape. The surface tension will generate internal flows to reduce the surface area, causing the droplet to deform towards a more spherical shape. As the oblate droplet begins to oscillate, the internal flows induced by surface tension forces are relatively strong, resulting in moderate viscous dissipation. During the deformation process, as the droplet transitions from an elongated shape toward a spherical one, a substantial internal velocity gradient develops. The fluid circulates within the droplet in response to capillary forces, particularly near the interfacial regions where the curvature changes rapidly. Viscous dissipation peaks at intermediate stages, when the droplet's shape is neither fully elongated nor fully spherical. These points correspond to the local minima in Fig. 7 (b), where the droplet undergoes rapid deformation, generating intense internal fluid motion and viscous stresses. As the droplet approaches a final spherical configuration, the internal velocity gradient diminishes, and the fluid motion gradually subsides due to viscous damping effects. Once the droplet reaches a near-spherical state, viscous dissipation significantly decreases. In this near-equilibrium condition, the internal fluid flows are minimal, resulting in a much lower dissipation rate. While being always negative,  $\dot{E}_{tot}^* \approx 0$  implies the equilibrium stage.

It is of paramount importance to mention that  $E_{tot}$  is obtained by Eq. (9). It encompasses both kinetic and mixing energies. Intuitively, the total energy of the two-phase flow comprises both kinetic and surface energies. As mentioned, the relationship between mixing and free energies is defined in Eq. (13) under

certain assumptions. In this work, we aim to provide a detailed analysis of the correlation between the two under general conditions. To calculate the surface energy, the interface profile is extracted as the isocontour of  $c = 0$  with ParaView software (Ayachit, 2015). For axisymmetric flows, the surface energy ( $E_s$ ) is calculated by multiplying the surface tension coefficient by the surface area:

$$E_s = 2\pi\gamma \int_{z_1}^{z_2} r(z) \sqrt{1 + \left(\frac{dr}{dz}\right)^2} dz. \quad (38)$$

The integration in Eq. (38) requires the interfacial profile data to be sorted for calculating the surface area. A nearest neighbor algorithm is utilized to achieve the necessary sorting of the interface profile data. The mixing energy  $E_m$  or free energy functional  $\mathcal{F}$  composed of bulk and gradient components is obtained by computing the volume integral in Eq. (7).

The results plotted in Fig. 8 (a) and Fig. 8 (b) show that reducing the interfacial thickness aids in reducing the difference between the mixing and surface energies. The largest difference, approximately 10%, occurs at the initial condition when the droplet exhibits the greatest aspect ratio and the highest curvature non-uniformity. For all capillary widths, the local maximum errors between the two occur at the peaks of the surface energy, while the local minimum errors are observed for aspect ratio equal to unity. This is related to the simplified assumptions used in linking the mixing energy to the surface energy. As the droplet nears its final spherical equilibrium state with uniform curvature, the gradient of the chemical potential vanishes, and the error decreases, indicating that the simplifying assumptions in Eq. (13) become more accurate in representing the surface energy.

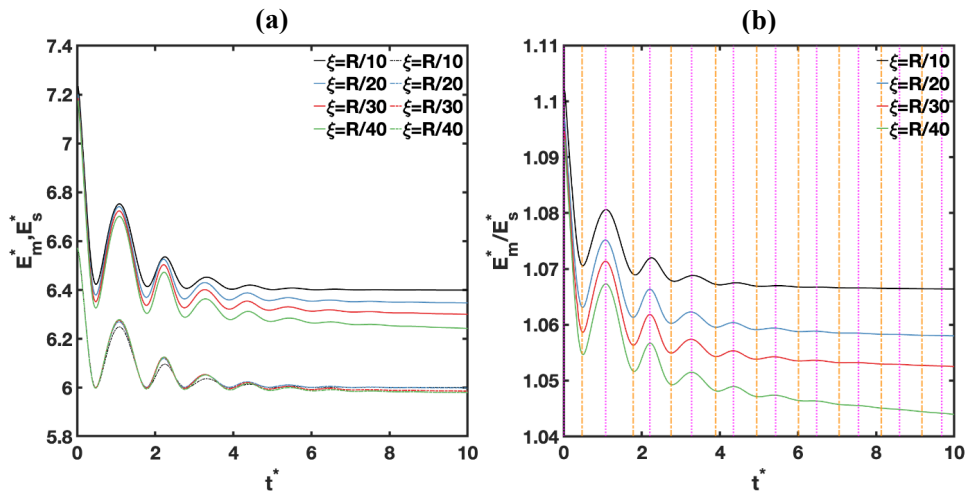


**Fig. 8.** Comparison between the mixing energy and traditional surface energy: (a) The corresponding non-dimensional values with solid lines representing mixing energy and dash-dotted lines indicating surface

energy, and (b) the ratio of mixing energy to surface energy as a function of capillary width. The magenta dotted lines indicate moments with maximum deformation, while the orange dash-dotted lines indicate when the aspect ratio is one.

### 6.3. Breakup of a cylindrical capillary jet

The breakup of a liquid thread is investigated using the diffuse interface approach. The temporal instability of an axisymmetric capillary jet is numerically simulated, triggered by an initial harmonic disturbance. The simulation protocol and boundary conditions follow the procedure established by Ashgriz and Mashayek (Ashgriz and Mashayek, 1995), who initially examined for the primary breakup in a vacuum. The phase-field variable initialization is given by the following tangent hyperbolic function in a square domain  $[0, \Lambda] \times [0, \Lambda]$ :

$$c(r, z, 0) = \tanh \frac{2 \left( R + \varepsilon_0 R \cos \left( \frac{2\pi z}{\Lambda} \right) - r \right)}{2\sqrt{2}\xi}, \quad (39)$$

where  $R$  is the radius of the jet;  $\varepsilon_0$  is the amplitude of the initial surface disturbance;  $\Lambda$  is the wavelength;  $\xi$  is the interfacial thickness, and  $k = 2\pi R/\Lambda$  is the wavenumber. The Reynolds and Weber numbers are defined similarly to those in the droplet oscillation problem, with values set to 10 ( $Re = 10$ ) and 1 ( $We = 1$ ), respectively. The initial disturbance amplitude is set to  $\varepsilon_0 = 0.05$ , and the wavenumber is  $k = 0.5$ . The density and viscosity ratios are selected as,  $\rho_1/\rho_2 = 100$  and  $\mu_1/\mu_2 = 10$ , respectively.

The study aims to investigate the dynamics of energy transfer at the breakup point and the oscillation behavior of the satellite droplet. Jet breakup is a crucial process in many scientific and engineering applications, such as spray atomization (Ashgriz, 2011; Cundy et al., 2024; Faeth et al., 1995). In spray atomization, bulk liquids are broken into fine droplets, significantly increasing surface area, which enhances efficiency in processes such as fuel combustion (Gemci and Chigier, 2016), targeted drug delivery (Shrestha et al., 2023), and surface coating applications (Jackiw and Ashgriz, 2021). Despite the latest advancements in the field, the interrelation between kinetic energy, surface energy, and viscous dissipation during droplet breakup has been the subject of only a few studies, if any. Another objective of the study is to quantify the kinetic energy in both the main and satellite droplets following the pinch-off. Most of the two-phase flow literature is concerned about the primary breakup. Due to the robustness of energy-based phase-field methods, they do not require special attention for complex topological changes such as droplet breakup and coalescence. To prevent the unphysical disappearance of satellite droplets with smaller radii, an adaptive time stepper is utilized to adjust the time step size to match the characteristic time of the satellite droplet after pinch-off. Employing this technique, the unphysical shrinkage of smaller droplets is effectively

handled. The initial profile of the capillary jet and some results before the primary breakup are given in Fig. 9 (a) and post-breakup in Fig. 9 (b).

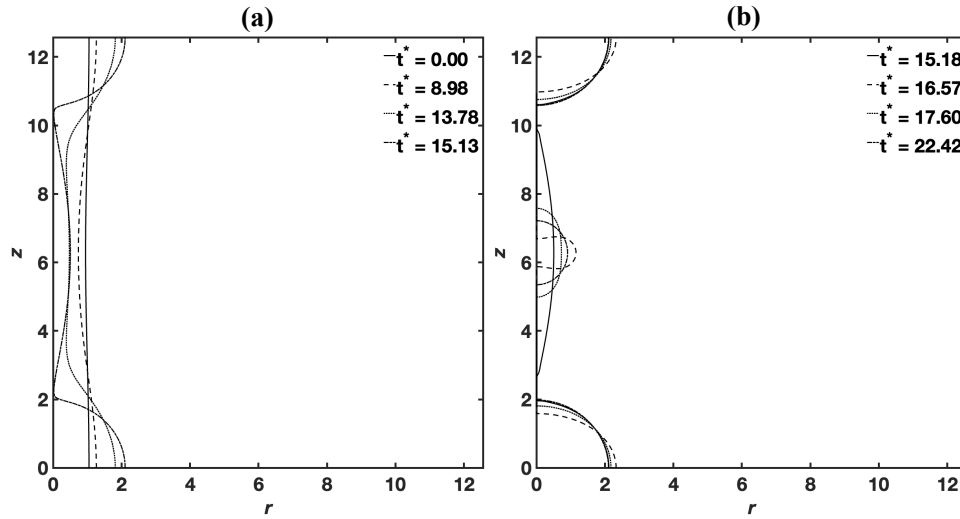


**Fig. 9.** The results for the breakup of a capillary jet. Time sequence of the harmonic perturbation growth for (a) primary breakup and (b) post-pinch-off.

Initially, the jet possesses maximum surface or mixing energy and zero kinetic energy, as shown in Fig. 10 (a) and Fig. 10 (b). As the disturbance grows, the kinetic energy of the flow continuously increases until  $t^* = 13.78$  and facilitates the nonlinear growth of the initial perturbation. At this point, the jet is rapidly converging towards the pinch-off point, and the fluid is accelerating due to surface tension forces driving the liquid from the thinner neck zone into thicker swell regions. It is observed that between  $t^* = 13.78$  and  $t^* = 15.04$ , as the flow converges towards the pinch-off point, the kinetic energy of the two-phase flow decreases.

At about  $t^* = 15.13$ , a singular point forms on the jet surface as the radius approaches zero and the curvature increases dramatically. This is roughly the moment when breakup occurs, accompanied by a significant increase in the kinetic energy. In addition to  $E_k^*$  and  $E_m^*$ , studying the time derivative of kinetic and mixing energies ( $\dot{E}_k^*$  and  $\dot{E}_m^*$ ) provides a significant physical insight into the jet breakup problem. From Fig. 10 (c) and (d), as soon as the jet breakup happens, the kinetic energy of the flow ( $E_k^*$ ) substantially increases. The maximum fluid velocity occurs near the pinch-off location at the breakup time and accelerates the satellite droplet after the primary breakup. It is observed that at the pinch-off time, the time derivative of the mixing energy ( $\dot{E}_m^*$ ) reaches its minimum value, meaning that the rate of the decrease in mixing/surface energy reaches its highest magnitude. Therefore, it is  $\dot{E}_m^*$  not  $E_m^*$ , that exhibits extrema at the breakup moment.  $E_m^*$  continues to decrease until the dynamics are dominated by the oscillation of the main and satellite droplets. Post-breakup, a smaller satellite droplet with high velocity and a larger main droplet with smaller velocity emerge. While comprehensive studies are available on the physics of the flow

prior to the primary breakup, the physics of the post-breakup are not well-understood, especially in the case of satellite droplet(s).

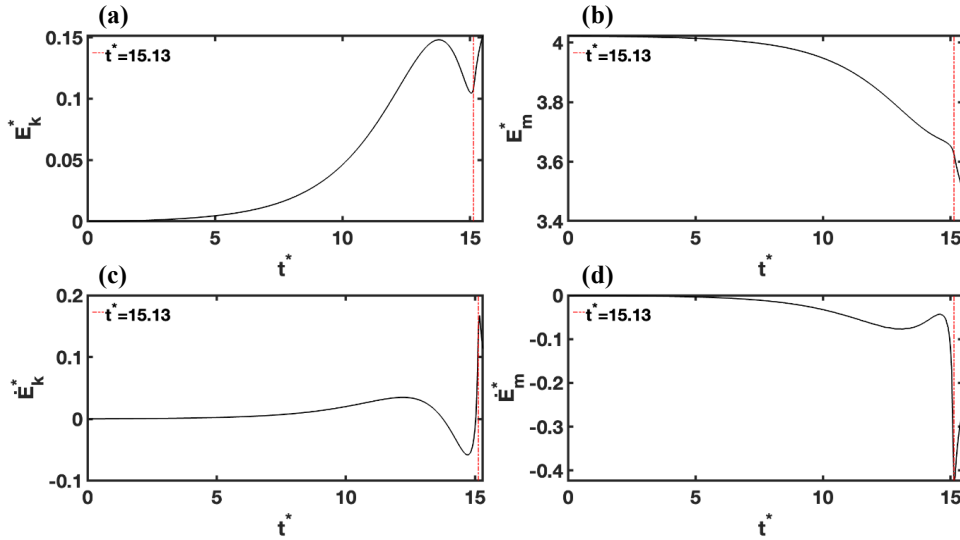


**Fig. 10.** The results for the temporal evolution of the (a) kinetic energy, (b) mixing energy, (c) time derivative of the kinetic energy and (d) time derivative of the mixing energy for the capillary jet breakup problem.

Numerous studies have been conducted on the dynamics of droplet oscillation, and it is well-known that the oscillation frequency is heavily influenced by the droplet's size (Fahimi et al., 2023; Rayleigh, 1879; Tsamopoulos and Brown, 1983). The varying Reynolds and Weber numbers associated with the oscillations of the main and satellite droplets pose a challenge for numerical solvers due to the multiphysics nature and differing time scales of the phenomena. This issue is carefully addressed by employing adaptive time steppers to match the time step size with the oscillation of the satellite droplet.

The results presented in Fig. 11 show the shape of the satellite droplet at various stages. The first oscillation period, measured as the time between the first and second maximum axial deformations during the oscillation, differs from subsequent periods. This stems first from the highly deformed shape of the droplet after the pinch-off, and second from the high value of  $\dot{E}_k^*$  at the breakup time. At  $t^* = 15.18$ , the ligament is long and thin, indicating that it has been stretched significantly. By  $t^* = 15.71$ , the shape has become more constricted, with a visible neck forming in the middle. This indicates the ligament is in the process of relaxing due to surface tension but is not undergoing further breakup. Between  $t^* = 15.71$  and  $t^* = 16.61$ , the ligament undergoes a remarkable transformation. As time progresses, the middle section narrows, and the ligament starts taking on a more rounded form. By  $t^* = 16.61$ , the shape adopts a distinct toroidal (donut-like) structure, indicating a transition state driven by surface tension. This toroidal shape signifies the retraction of the fluid body, as it moves toward a stable configuration before ultimately forming

a spherical droplet. After the first oscillation period, the satellite droplet undergoes regular transitions between oblate and prolate spheroidal shapes. The oscillations continue until the droplet quickly stabilizes into its final equilibrium, adopting a spherical shape.

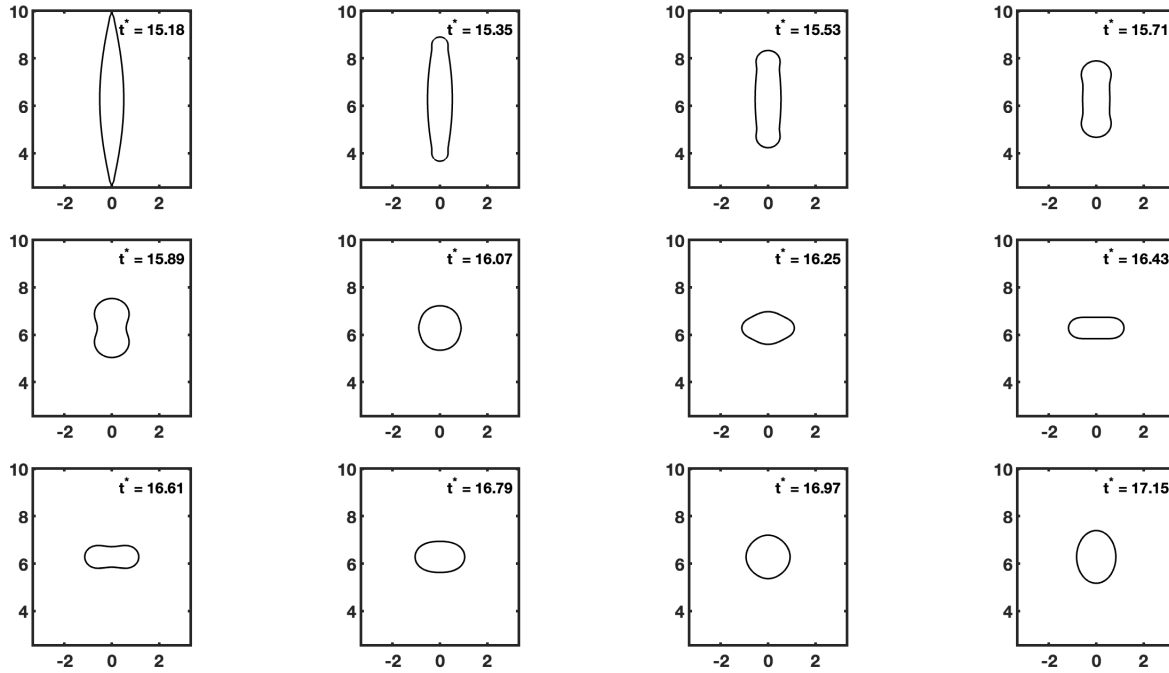


**Fig. 11.** Time sequence of the oscillations of the satellite droplet post-pinch-off.

The total kinetic energies of the main and satellite droplets displayed in Fig. 12 confirm the varying temporal scales of the motion between the main and satellite droplets. Before the breakup, the high curvature at the pinch-off point generates a significant pressure gradient, accelerating the fluid and resulting in a high velocity at the satellite droplet's tip. Post-breakup, the main droplet exhibits alternating transitions between oblate and prolate shapes. By contrast, the satellite droplet becomes highly deformed, reaching a state where nonlinear effects distort its shape into a toroidal form. Consequently, the differences in fluid velocity, along with size and shape disparities, contribute to the distinct time scales of motion between the satellite droplet and the main droplet. Both droplets attempt to adjust into a spherical shape, minimizing their surface area and energy. Therefore, the post-pinch-off phase can be regarded as a dual droplet oscillation problem, with two distinct scales of motion where the competition between kinetic energy, surface energy, and viscous dissipation dictates their dynamics.

The results in Fig. 12 imply that right after the primary breakup, the satellite droplet holds nearly 28% of the total kinetic energy while carrying only 17% of the total mass of the original jet. The figure indicates that the first oscillation of the satellite droplet is accompanied by the highest increase in the kinetic energy, corresponding to a decrease in the surface energy. At  $t^* = 15.98$  where the satellite droplet reaches its maximum kinetic energy, it accounts for 88% of the total kinetic energy. Due to the lower Reynolds number

associated with the satellite droplet, resulting from its smaller size, its oscillations are faster and dampened much more quickly than those of the main droplet. The results for the kinetic energy indicate that all periods of the oscillation for the satellite droplet are smaller than the main droplet. After five oscillations, the satellite droplet ceases its motion and reaches an equilibrium state by  $t^* = 22$ . On the other hand, the main droplet continues to oscillate, with its motion persisting even beyond  $t^* = 36$ , retaining all the kinetic energy from the pinched-off jet. The observed pattern is attributable to the higher Reynolds number of the main droplet's oscillations and the reduced impact of viscous forces.

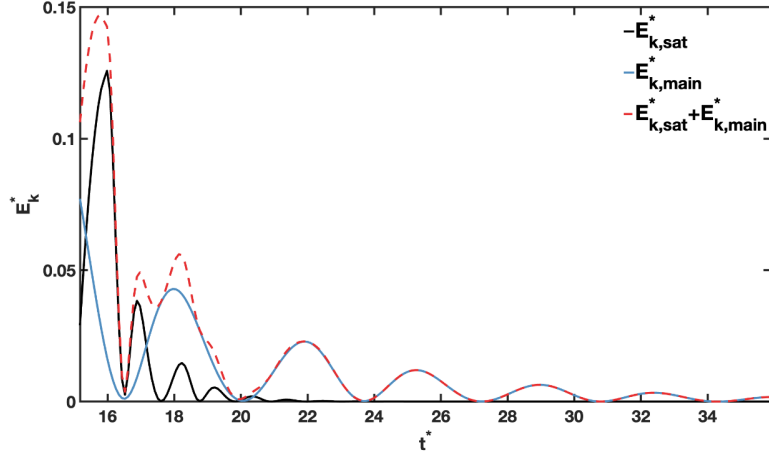


**Fig. 12.** The temporal variation of the kinetic energy of the main and satellite droplets, along with their combined total kinetic energy.

The final objective of this study is to provide a comparison between the  $\int_0^t \int_{\Omega} \mathbf{u} \cdot \mathbf{F}_{st} d\Omega dt$ , which essentially indicates the work of surface tension force, and its relation to changes in mixing and surface energies. This test is one way to quantitatively assess the accuracy of the surface tension force derived from the Korteweg stress tensor (Eq. (18)) in representing the changes in surface/mixing energy.

The results displayed in Fig. 13 compare the non-dimensional  $\int_0^t \int_{\Omega} \mathbf{u} \cdot \mathbf{F}_{st} d\Omega dt$ ,  $\Delta E_m^*$  and  $\Delta E_s^*$ . At the initial stage where the jet has a flat profile with a small harmonic disturbance, variables remain indistinguishable. As the jet develops and the curvature changes across the jet interface, the disparity between  $\Delta E_m^*$  and  $\Delta E_s^*$  increases. Despite this, by providing sufficient mesh resolution using AMR, the work of the surface tension force and  $\Delta E_m^*$  match excellently throughout the entire computational period. Overall, the findings from this and the preceding section suggest that the accuracy of Eq. (12) in estimating surface energy is highly dependent on the interface profile. Providing sufficient mesh resolution, it was shown that for spherical interface in droplet oscillation and flat interface in jet breakup the errors are smaller. When the interface curvature is non-uniform, the error increases. It reaches its peak, where the curvature exhibits the greatest non-uniformity along the interfacial profile.



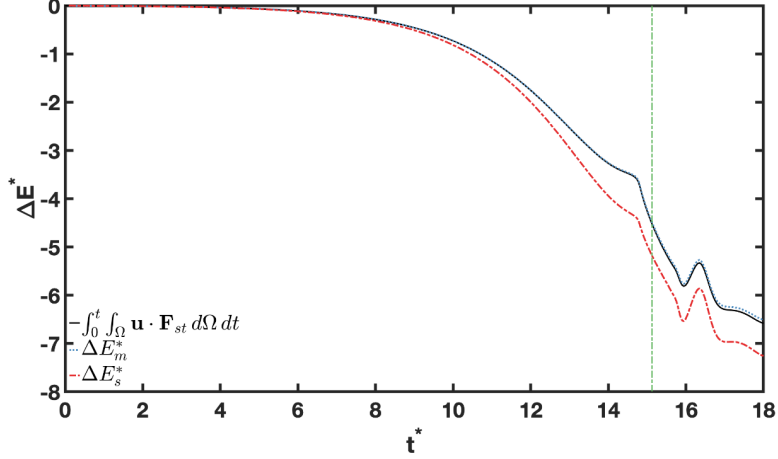


**Fig. 13.** Comparison between the non-dimensional work of surface tension force and the change in mixing energy and surface energy for  $\xi = R/30$ . The green dash-dotted line shows the breakup moment.

## 7. Conclusions

This work provides a comprehensive energy-based perspective on two-phase flows modeled using the coupled CHNS equations. By ensuring energy conservation in the numerical framework, this study highlights the critical role of energy balance in interpreting two-phase flow dynamics. The energy equation, derived from the momentum balance equation, serves as the foundation for this analysis, offering insights into the interplay between kinetic energy, mixing energy, and viscous dissipation.

A central focus of the study is the comparison between the mixing energy and the surface energy. It is found that the coupling between these energies is highly accurate for interfaces with uniform curvature, while errors increase with greater curvature non-uniformity. The energy-based surface tension formulation, derived from the Korteweg stress tensor, effectively represents variations in the mixing energy, further validating its robustness for modelling complex interfacial flows.

The dynamics of droplet oscillations and capillary jet breakup are investigated as benchmark tests, revealing new insights into two-phase flow behavior. For droplet oscillations, the findings confirm that reducing the interfacial thickness enhances the convergence of energy components, enabling an accurate characterization of the interaction between the kinetic energy, viscous dissipation, and mixing energy. For capillary jet breakup, the analysis highlights distinct energy transfer mechanisms at the moment of breakup, notably the rise in kinetic energy and the simultaneous sharp decrease in mixing energy. Post-breakup, the satellite droplet dynamics exhibit notably faster oscillation damping due to its smaller Reynolds number, contrasting with the persistent oscillations of the primary droplet.

The time derivative of the total energy functional emerges as a powerful tool for identifying dissipative flow stages, providing detailed information about energy transfer mechanisms. This study not only

examines two-phase flows from an energy standpoint but also offers practical methodologies to ensure numerical consistency and accuracy in terms of energy balance. Future work will extend the energy-based approach to incorporate additional physical phenomena, including gravity, Marangoni effects (Mostafavi et al., 2024a), thermal effects, and electric field.

## Acknowledgements

The authors acknowledge the financial support from the National Science Foundation awards CBET 2312197 and 2224749. Simulations were performed using the High-Performance Computing (HPC) resources supported by the University of Arizona TRIF, UITS, and Research, Innovation, and Impact (RII) and maintained by the University of Arizona Research Technologies team.

## References

- Abels, H., Garcke, H., Grün, G., 2012. Thermodynamically consistent, frame indifferent diffuse interface models for incompressible two-phase flows with different densities. *Math. Models Methods Appl. Sci.* 22, 1150013. <https://doi.org/10.1142/S0218202511500138>
- Allen, S.M., Cahn, J.W., 1972. Ground state structures in ordered binary alloys with second neighbor interactions. *Acta Metall.* 20, 423–433. [https://doi.org/10.1016/0001-6160\(72\)90037-5](https://doi.org/10.1016/0001-6160(72)90037-5)
- Alvarado, V., Manrique, E., 2010. Enhanced Oil Recovery: An Update Review. *Energies* 3, 1529–1575. <https://doi.org/10.3390/en3091529>
- Anderson, D.M., McFadden, G.B., Wheeler, A.A., 1998. DIFFUSE-INTERFACE METHODS IN FLUID MECHANICS. *Annu. Rev. Fluid Mech.* 30, 139–165. <https://doi.org/10.1146/annurev.fluid.30.1.139>
- Ashgriz, N., 2011. *Handbook of Atomization and Sprays: Theory and Applications*. Springer Science & Business Media.
- Ashgriz, N., Mashayek, F., 1995. Temporal analysis of capillary jet breakup. *J. Fluid Mech.* 291, 163–190. <https://doi.org/10.1017/S0022112095002667>
- Ayachit, U., 2015. *The ParaView Guide: A Parallel Visualization Application*. Kitware, Inc., Clifton Park, NY, USA.
- Brackbill, J.U., Kothe, D.B., Zemach, C., 1992. A continuum method for modeling surface tension. *J. Comput. Phys.* 100, 335–354. [https://doi.org/10.1016/0021-9991\(92\)90240-Y](https://doi.org/10.1016/0021-9991(92)90240-Y)
- Cahn, J.W., Hilliard, J.E., 1958. Free Energy of a Nonuniform System. I. Interfacial Free Energy. *J. Chem. Phys.* 28, 258–267. <https://doi.org/10.1063/1.1744102>
- Chiu, P.-H., Lin, Y.-T., 2011. A conservative phase field method for solving incompressible two-phase flows. *J. Comput. Phys.* 230, 185–204. <https://doi.org/10.1016/j.jcp.2010.09.021>
- Cundy, C., Mirjalili, S., Laurent, C., Ermon, S., Iaccarino, G., Mani, A., 2024. A physics-informed machine learning model for the prediction of drop breakup in two-phase flows. *Int. J. Multiph. Flow* 180, 104934. <https://doi.org/10.1016/j.ijmultiphaseflow.2024.104934>
- Ding, H., Spelt, P.D.M., 2007. Wetting condition in diffuse interface simulations of contact line motion. *Phys. Rev. E* 75, 046708. <https://doi.org/10.1103/PhysRevE.75.046708>
- Eyre, D.J., 1998. Unconditionally Gradient Stable Time Marching the Cahn-Hilliard Equation. *MRS Online Proc. Libr. OPL* 529, 39. <https://doi.org/10.1557/PROC-529-39>
- Faeth, G.M., Hsiang, L.-P., Wu, P.-K., 1995. Structure and breakup properties of sprays. *Int. J. Multiph. Flow, Annual Reviews in Multiphase Flow* 1995 21, 99–127. [https://doi.org/10.1016/0301-9322\(95\)00059-7](https://doi.org/10.1016/0301-9322(95)00059-7)

- Fahimi, K., Mädler, L., Ellendt, N., 2023. Measurement of surface tension with free-falling oscillating molten metal droplets: a numerical and experimental investigation. *Exp. Fluids* 64, 133. <https://doi.org/10.1007/s00348-023-03678-9>
- Gaston, D., Newman, C., Hansen, G., Lebrun-Grandié, D., 2009. MOOSE: A parallel computational framework for coupled systems of nonlinear equations. *Nucl. Eng. Des.* 239, 1768–1778. <https://doi.org/10.1016/j.nucengdes.2009.05.021>
- Gbadamosi, A.O., Junin, R., Manan, M.A., Agi, A., Yusuff, A.S., 2019. An overview of chemical enhanced oil recovery: recent advances and prospects. *Int. Nano Lett.* 9, 171–202. <https://doi.org/10.1007/s40089-019-0272-8>
- Gemci, T., Chigier, N., 2016. Atomization, Spraying, and Nebulization, in: Merkus, H.G., Meesters, G.M.H. (Eds.), *Production, Handling and Characterization of Particulate Materials*. Springer International Publishing, Cham, pp. 201–256. [https://doi.org/10.1007/978-3-319-20949-4\\_7](https://doi.org/10.1007/978-3-319-20949-4_7)
- Halder, S., Granda, R., Wu, J., Sankaran, A., Yurkiv, V., Yarin, A.L., Mashayek, F., 2022. Air bubble entrapment during drop impact on solid and liquid surfaces. *Int. J. Multiph. Flow* 149, 103974. <https://doi.org/10.1016/j.ijmultiphaseflow.2022.103974>
- Hirt, C.W., Nichols, B.D., 1981. Volume of fluid (VOF) method for the dynamics of free boundaries. *J. Comput. Phys.* 39, 201–225. [https://doi.org/10.1016/0021-9991\(81\)90145-5](https://doi.org/10.1016/0021-9991(81)90145-5)
- Hua, J., Lin, P., Liu, C., Wang, Q., 2011. Energy law preserving C0 finite element schemes for phase field models in two-phase flow computations. *J. Comput. Phys.* 230, 7115–7131. <https://doi.org/10.1016/j.jcp.2011.05.013>
- Jackiw, I.M., Ashgriz, N., 2021. On aerodynamic droplet breakup. *J. Fluid Mech.* 913, A33. <https://doi.org/10.1017/jfm.2021.7>
- Jacqmin, D., 1999. Calculation of Two-Phase Navier–Stokes Flows Using Phase-Field Modeling. *J. Comput. Phys.* 155, 96–127. <https://doi.org/10.1006/jcph.1999.6332>
- Jain, S.S., Mani, A., Moin, P., 2020. A conservative diffuse-interface method for compressible two-phase flows. *J. Comput. Phys.* 418, 109606. <https://doi.org/10.1016/j.jcp.2020.109606>
- Karypis, G., Kumar, V., 1997. METIS—A Software Package for Partitioning Unstructured Graphs, Partitioning Meshes and Computing Fill-Reducing Ordering of Sparse Matrices.
- Khanwale, M.A., Saurabh, K., Ishii, M., Sundar, H., Rossmanith, J.A., Ganapathysubramanian, B., 2023. A projection-based, semi-implicit time-stepping approach for the Cahn-Hilliard Navier-Stokes equations on adaptive octree meshes. *J. Comput. Phys.* 475, 111874. <https://doi.org/10.1016/j.jcp.2022.111874>
- Kirk, B.S., Peterson, J.W., Stogner, R.H., Carey, G.F., 2006. libMesh: a C++ library for parallel adaptive mesh refinement/coarsening simulations. *Eng. Comput.* 22, 237–254. <https://doi.org/10.1007/s00366-006-0049-3>
- Lohse, D., 2022. Fundamental Fluid Dynamics Challenges in Inkjet Printing. *Annu. Rev. Fluid Mech.* 54, 349–382. <https://doi.org/10.1146/annurev-fluid-022321-114001>
- Mashayek, F., Ashgriz, N., 1995. A Spine-Flux Method for Simulating Free Surface Flows. *J. Comput. Phys.* 122, 367–379. <https://doi.org/10.1006/jcph.1995.1222>
- Mirjalili, S., Ivey, C.B., Mani, A., 2020. A conservative diffuse interface method for two-phase flows with provable boundedness properties. *J. Comput. Phys.* 401, 109006. <https://doi.org/10.1016/j.jcp.2019.109006>
- Mirjalili, S., Khanwale, M.A., Mani, A., 2023. Assessment of an energy-based surface tension model for simulation of two-phase flows using second-order phase field methods. *J. Comput. Phys.* 474, 111795. <https://doi.org/10.1016/j.jcp.2022.111795>
- Mostafavi, A., Ranjbar, M., Yurkiv, V., Yarin, A., Mashayek, F., 2024a. Mass-conserving Phase-Field Numerical Simulation of Surfactant-induced Two-phase Flows. *Bull. Am. Phys. Soc.*
- Mostafavi, A., Ranjbar, M., Yurkiv, V.R., Yarin, A.L., Mashayek, F., 2024b. Moose-Based Finite Element Framework for Mass-Conserving Two-Phase Flow Simulations on Adaptive Grids Using the Diffuse Interface Approach and a Lagrange Multiplier. <https://doi.org/10.2139/ssrn.4890110>

- Mostafavi, A., Saidi, S., Moghtaderi, M., 2024c. Three-Dimensional Simulation of Circulating Tumor Cells Magnetic Isolation Using a Viscoelastic-Based Ferrofluid Solution. <https://doi.org/10.2139/ssrn.4898904>
- Mostafavi, A., Yurkiv, V., Yarin, A., Mashayek, F., 2023. Three-dimensional phase-field modeling of the drop impact on a solid superhydrophobic flat surface. *Bull. Am. Phys. Soc.*
- Permann, C.J., Gaston, D.R., Andrš, D., Carlsen, R.W., Kong, F., Lindsay, A.D., Miller, J.M., Peterson, J.W., Slaughter, A.E., Stogner, R.H., Martineau, R.C., 2020. MOOSE: Enabling massively parallel multiphysics simulation. *SoftwareX* 11, 100430. <https://doi.org/10.1016/j.softx.2020.100430>
- Peterson, J.W., Lindsay, A.D., Kong, F., 2018. Overview of the incompressible Navier–Stokes simulation capabilities in the MOOSE framework. *Adv. Eng. Softw.* 119, 68–92. <https://doi.org/10.1016/j.advengsoft.2018.02.004>
- Ranjbar, M., Mostafavi, A., Rajendran, P.T., Komperda, J., Mashayek, F., 2024. Modal analysis of turbulent flows simulated with spectral element method. *Phys. Fluids* 36, 125164. <https://doi.org/10.1063/5.0234014>
- Rayleigh, Lord, 1879. On the capillary phenomena of jets. *Proc. R. Soc. Lond.* 71–97.
- RUBINSTEIN, J., STERNBERG, P., 1992. Nonlocal reaction—diffusion equations and nucleation. *IMA J. Appl. Math.* 48, 249–264. <https://doi.org/10.1093/imamat/48.3.249>
- Rump, M., Saade, Y., Sen, U., Fezzaa, K., Versluis, M., Lohse, D., Segers, T., 2022. Vorticity-induced flow-focusing leads to bubble entrainment in an inkjet printhead: Synchrotron x-ray and volume-of-fluid visualizations. *Phys. Rev. Fluids* 7, 104004. <https://doi.org/10.1103/PhysRevFluids.7.104004>
- Shen, J., Tang, T., Yang, J., 2016. On the maximum principle preserving schemes for the generalized Allen–Cahn equation. *Commun. Math. Sci.* 14, 1517–1534. <https://doi.org/10.4310/CMS.2016.v14.n6.a3>
- Shen, J., Xu, J., Yang, J., 2018. The scalar auxiliary variable (SAV) approach for gradient flows. *J. Comput. Phys.* 353, 407–416. <https://doi.org/10.1016/j.jcp.2017.10.021>
- Shen, J., Yang, X., 2015. Decoupled, Energy Stable Schemes for Phase-Field Models of Two-Phase Incompressible Flows. *SIAM J. Numer. Anal.* 53, 279–296. <https://doi.org/10.1137/140971154>
- Shrestha, K., Van Strien, J., Fletcher, D.F., Inthavong, K., 2023. Primary spray breakup from a nasal spray atomizer using volume of fluid to discrete phase model. *Phys. Fluids* 35, 053312. <https://doi.org/10.1063/5.0150890>
- Sussman, M., Smereka, P., Osher, S., 1994. A Level Set Approach for Computing Solutions to Incompressible Two-Phase Flow. *J. Comput. Phys.* 114, 146–159. <https://doi.org/10.1006/jcph.1994.1155>
- Tsamopoulos, J.A., Brown, R.A., 1983. Nonlinear oscillations of inviscid drops and bubbles. *J. Fluid Mech.* 127, 519–537. <https://doi.org/10.1017/S0022112083002864>
- Xia, H., Lu, J., Dabiri, S., Tryggvason, G., 2018. Fully resolved numerical simulations of fused deposition modeling. Part I: fluid flow. *Rapid Prototyp. J.* 24, 463–476. <https://doi.org/10.1108/RPJ-12-2016-0217>
- Yang, X., 2016. Linear, first and second-order, unconditionally energy stable numerical schemes for the phase field model of homopolymer blends. *J. Comput. Phys.* 327, 294–316. <https://doi.org/10.1016/j.jcp.2016.09.029>
- Yarin, A.L., 2006. DROP IMPACT DYNAMICS: Splashing, Spreading, Receding, Bouncing.... *Annu. Rev. Fluid Mech.* 38, 159–192. <https://doi.org/10.1146/annurev.fluid.38.050304.092144>
- Yue, P., 2020. Thermodynamically consistent phase-field modelling of contact angle hysteresis. *J. Fluid Mech.* 899, A15. <https://doi.org/10.1017/jfm.2020.465>
- Yue, P., Feng, J.J., Liu, C., Shen, J., 2004. A diffuse-interface method for simulating two-phase flows of complex fluids. *J. Fluid Mech.* 515, 293–317. <https://doi.org/10.1017/S0022112004000370>
- Zhao, B., MacMinn, C.W., Juanes, R., 2016. Wettability control on multiphase flow in patterned microfluidics. *Proc. Natl. Acad. Sci.* 113, 10251–10256. <https://doi.org/10.1073/pnas.1603387113>

Zhu, Q., Yan, J., 2021. A mixed interface-capturing/interface-tracking formulation for thermal multi-phase flows with emphasis on metal additive manufacturing processes. *Comput. Methods Appl. Mech. Eng.* 383, 113910. <https://doi.org/10.1016/j.cma.2021.113910>